Hypo-toxicity and prominent passivation characteristics of 316L stainless steel fabricated by direct metal laser sintering in a simulated inflammation environment

Xiaoqi Yue[a, b], Lei Zhang[a]*, Xiaoyan He[c, d], Decheng Kong[a], and Yong Hua[d]*

a: Corrosion and Protection Centre, University of Science and Technology Beijing, Beijing, 100083, China.
b: Shunde Graduate School, University of Science and Technology Beijing, Foshan, 528399, China
c: Reliability Engineering Institute, National Engineering Research Center for Water Transport Safety, Wuhan University of Technology, Wuhan 430063, China
d: Institute of Functional Surfaces, School of Mechanical Engineering, University of Leeds, Leeds, LS2 9JT, United Kingdom.

*Corresponding author: Yong Hua, Tel: +44 (0) 7923359918, fax: +44 (0) 1132424611.
Email: y.hua@leeds.ac.uk
Lei Zhang, Tel: +(010)62334410, fax: +(010)62334410.
Email: zhanglei@ustb.edu.cn

Abstract

3D-printing is an emerging technology that challenged wrought counterparts by one-step manufacturing for complicated biological devices. However, the material properties and surface features due to manufacturing parameters play an important role on the corrosion behaviour and influence the toxicity of the material as an implant. In this paper, the improvement of pitting potential was observed by electrochemical experiments as the result of grain refinement of DMLS 316L at 200W laser power. The ICP results verified the supressed release of toxic cations after the formation of the passive film with enhanced characteristics. However, the pores from DMLS 316L have the potential to develop into pits when polarised above pitting potential, promoting the risk of using 3D-printed 316L as implant materials.

Keywords: inflammation, 3D-printing implant, passive film, hypo-toxicity, porosity

1.0 Introduction

316L Stainless Steel (SS) is recognised as having good mechanical properties and excellent corrosion resistance, which has been commonly used in medical implants for decades. The traditional processing for implantable medical devices, such as dental implants, orthopedic implants, and coronary stents, is manufactured via multiple machining processes after quenched moulding. The manufacturing process becomes simplify with the arrival of the laser powder bed fusion (LPBF) method for such biometal applications [1,2]. The LPBF process permits the one-step fabrication of complex components with relatively low residual stress and can achieve good tensile strength via rapid cooling [3].

For 316L SS, the dissolution of the metal ions such as Cr^{3+}, Fe^{2+} and Ni^{2+}, etc in a passivation state [4–6] can be accelerated due to the deterioration of the environments, such as concentrated corrosive ions or high temperature [7]. Inflammatory response, which is an inevitable stage after the implantation of a metal device, producing aggressive body conditions with acidic pH, superoxide radicals, and higher body temperatures [8,9]. Many studies have reported the corrosion behavour of 316L SS in the inflammatory response and concluded that the levels of H_2O_2 became rapidly concentrated and elevated from 3.6 to 150000 ppm, followed by a pH decreased from 7.4 to 5.2 [10,11]. Atapour et al. [12] investigated the corrosion behaviour and the release of metal ions from laser melted 316L SS in a synthetic physiological fluid containing proteins, they found that 3D-printed showed a lower pitting susceptibility compared to the wrought 316L SS. H_2O_2 demonstrated to decrease the corrosion resistance of 316L SS as the implant materials [9,10,13], leading to an increase

of the released metal ions, especially for Ni [14,15]. This has been attributed to the additional reactions between metal ions and strong oxidant H_2O_2, and the corrosion products have been proposed as a high valence compound [16–18].

The release of metal ions from implants during corrosion reactions causes adverse tissue reactions, which ultimately require surgical revision to the implants. It has been proved that the decrease of nickel content in SS effectively decreased the allergic response of tissues [19]. Chromium, iron, and molybdenum, which are more active than nickel, and preferentially oxidized to form the passive film [20]. Metikoš [21] indicated that the concentration of Cr ions was extremely low peri-implants and mainly consumed in forming Cr_2O_3 and $Cr(OH)_3$. Iron also preferred to form compounds whereas less stable than chromium compounds. The elevated level of chromium and iron ions was related to the degradation of the passive film via surface acidification [7,22–27]. On the contrary, the molybdenum was favourable to dissolve at high pH [28,29]. Waleed et al. [30] evaluated the cytotoxicity of elemental ions and found that the cytotoxicity of molybdenum was weak even in a tenfold higher concentration of the tested solution. Among them, nickel was considered as the most toxic element, followed by iron and chromium [30,31].

The nickel-reduced SS alloys were proposed to reduce the allergic response. However, their magnetic properties and deteriorated corrosion resistance narrowed the application [32]. Recent studies indicated that the 316L SS manufactured by LPBF provided good biocompatible performance and excellent corrosion resistance [33,34]. Kong et al. [35] pointed out that the LPBF 316L SS exhibited better performance and quality with the increase in the laser power. Our previous work also revealed that the LPBF 316L SS via 200 W laser power exhibited

excellent passivation behaviour compared to that of the wrought 316L SS in a PBS solution [36]. The dense and compact passive film naturally formed on the LPBF 316L SS surface contains a higher proportion of chromium oxide than that of the passive film formed on the wrought 316L SS surface, which improves corrosion resistance and decreases the total mass loss during the exposure. Al-Mamun et al. [37] also proposed that the refined sub-grains within each coarse grain and the restriction of forming micro-inclusions (MnS etc.) improves the passivation behaviours. However, understanding the release of hazardous metal ions such as Ni from LPBF 316L SS in a body fluid remains a controversy. Kong et al. [35] revealed that the release of Ni was favoured to be as metal ions rather than compounds within the passive film during the simulated immersion process. Xu et al. [10] reported that the composition of passive film formed on wrought 316L SS in physiological saline, showing identified metallic nickel within the passive film after 16 weeks immersion. Recently, Man et al. [34] identified the formation of divalent nickel compound in the passive film for 316L SS, suggesting that high Ni compounds within the passive film can depress the Ni release to the solution. There is insufficient work for the role of toxicity in the application of LPBF 316L SS as implants, especially through the complicated inflammation periods are rare and this has hampered the process of the practicality for LPBF biomaterials.

Therefore, the objective of this research work is to fill the knowledge gap for evaluation of the toxicity and passivation behaviours of LPBF manufactured 316L SS (Direct Metal Laser Sintering, DMLS), evaluating the corrosion behaviour of DMLS and wrought 316L SS in an aggressive inflammatory condition and revealed the toxicity of DMLS and wrought 316L SS in the early stages of implantable immune inflammation. Electrochemical measurements,

surface analysis and surface profilometry were applied in establishing a relationship between the initial pores due to the 3D-printing process and pits growth on the surface as well as the release of metal ions and test duration influence the corrosion properties of DMLS and wrought 316L SS.

2.0 Experimental procedure

2.1 Materials and solution

The chemical compositions of wrought 316L SS (TISCO Steel via cold rolling) and 316L SS powder (Shanghai Engineering Research Center of 3D Printing Materials) used for DMLS are listed in Table 1, and the powder diameters are in the ranges of 15-45 μm. The 3D printed samples were produced via EOS M290 system; the printing parameters are described in Table 2. The powder layers were scanned in a continuous laser mode according to a zigzag pattern with inconstant volumetric energy density, each constructing layer was rotated by 67^{o} to reduce the stress concentration during manufacturing processes [35,38]. The wrought 316L SS was conducted by solution anneal treated at 1080^{o}C for 10 h followed by a water quench and cold rolling. All the samples were manufactured to a cylinder with a diameter of 10 mm and then cut uniformly to the thickness of 3mm. All samples were sealed in resin to leave one surface with an exposure area of 0.785 cm^2 to the solution. The sample surface was polished by using SiC paper up to 1000# grit, cleaned with acetone, ethanol, and DI water, respectively. The prepared samples were stored in a desiccator for 24 hours prior to each test.

Table 1. Chemical composition of wrought and powder 316L SS

Elements (wt%)	C	Cr	Mn	Si	P	S	Mo	Ni	N	Fe
Wrought 316L	0.03	17.5	2	1	0.045	0.03	2.5	13	0.11	Bal.
Powder 316L	0.02	16.8	1.9	0.1	0.032	0.02	2.25	12.1	0.15	Bal.

Table 2. Detailed printing parameters used in this work.

Baseplate temperature/^{o}C	Laser power/W	Scanning rate/mm·s^{-1}	Hatch distance/ µm	Powder thickness/µm
80	80/200	1083	90	25

Three types of solution were used to simulate the inflammation processes after implantation. The chemical compositions of the solution are listed in Table 2 and all tests were carried out at a constant temperature of 37±0.1^{o}C.

The solution in Stage 1 was based on the levels of H_2O_2 rapidly producing from superoxide in the inflammation processes [17,39,40]; the acidification (J.T. Baker) was simulated in Stage 2 [9]. Stage 3 has corresponded to the natural body environment which indicates the end of the inflammation process. The experiments from Stage1 to Stage 3 are to clarify the corrosion behaviour of the implant materials during the full-inflammation periods.

Table 2. Chemical composition of PBS solution

Concentration (mmol/L)	NaCl	KCl	Na_2HPO_4	KH_2PO_4	30%H_2O_2	pH
Stage 1	137	2.7	10	1.8	150	7.4
Stage 2	137	2.7	10	1.8	150	5.2

Stage 3	137	2.7	10	1.8	0	7.4

The simulated immersion tests for wrought 316L, DMLS 80W 316L, and DMLS 200W 316L SS were carried out in three stages, and the schematic diagram is provided in Figure 1. It is noted that the samples were not contacted with air as switching the solution between each stage.

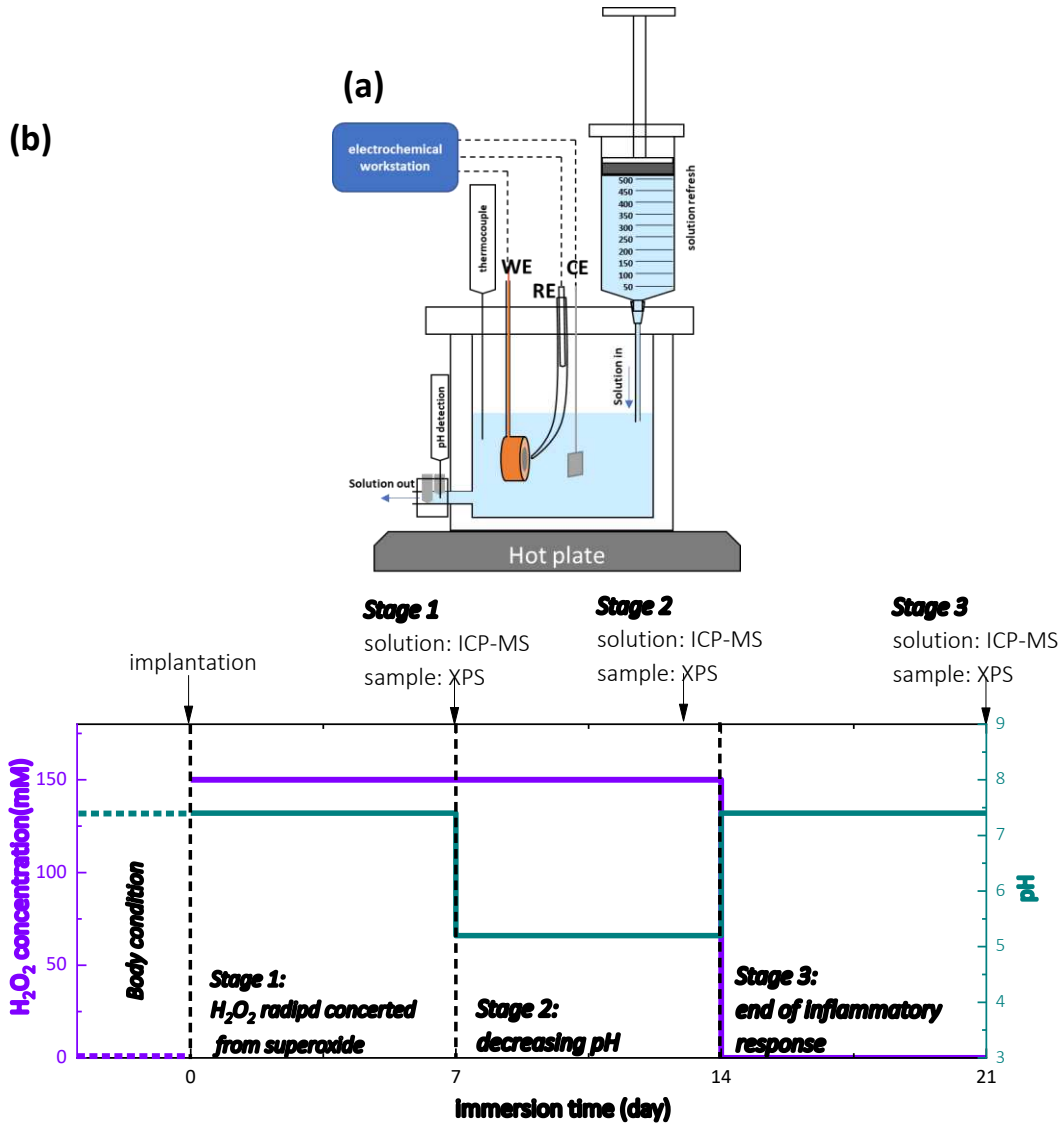

Figure 1. (a) Schematic diagram of the system. (b) Immersion tests in three consecutive stages (Stage1, Stage 2 and Stage 3 as shown in Table 2).

2.2 Methods

Electrochemistry measurements

The passivation behaviours of 316L SS manufactured through wrought and DMLS processes in

three types of simulated inflammation solutions were measured by potentiodynamic polarisation using a Gamry workstation in a conventional three-electrode cell, where platinum foil as the counter and Ag/AgCl as the reference electrodes respectively. Potentiodynamic polarisation was conducted via applying an anodic potential of 600 mV vs. Ag/AgCl potentiostatic for 4000 s after 1 hour of Open Circuit Potential (OCP) measurement and was initiated from -0.1 V vs OCP at a scanning rate of 0.5 mV/s. The reversed current density is 5 mA/cm^2 and the repassivation behaviour for localized corrosion susceptibility was measured according to ASTMG61 [41]. The potentiostatic polarisation tests were conducted by applying the anodic potential of 600 mV vs. Ag/AgCl for 4000 s.

The long-term Electrochemical Impedance Spectroscopy (EIS) measurements were monitored in various simulated inflammation solutions at OCP condition over a frequency range of 100 kHz to 10 mHz using 10 mV sinusoidal potential modulation. Both OCP and EIS measurements were continuously monitored on the same sample for all three stages.

Toxicity and surface characterisation

The surface characterisation was observed using OXFORD Nordlys MAX3 with a High-resolution CCD of 640 x 480. The concentration of Fe, Cr, Mo, and Ni ion releases in each period were measured and compared for various materials by Inductively Coupled Plasma – Mass Spectrometry (ICP-MS, Agilent 7500cc, USA). The X-Ray Photoelectron Spectroscopy (XPS, ESCALAB, 250XI) with an Al Kα X-ray source (hv=1486.6 eV) was operated by the end of each stage to identify the composition of surface passive films. The XPS spectra were calibrated by C1s peak at 284.8 eV, and the curves were fitted using an XPSPEAK4.1 software package. The profilometry was performed on the surface to charactersation of the pores/pit

163 at each stage.

164 ## *3.0 Results*

165 ### *3.1 Characterisation of material microstructure*

166 Figure 2 shows the grain sizes and surface morphologies of wrought 316L SS and DMLS 316L
167 SS manufactured by DMLS at 80W and 200W, respectively. The DMLS 316L SS samples indicate
168 that fine grains are surrounded by irregular grains. Both DMLS 80W and 200W 316L SS show
169 smaller grain sizes and their sizes are elongate along the constructed direction, while large
170 and regular grains are found for wrought 316L SS. It is also noted that pores exist on the 80 W
171 DMLS sample as shown in Figure 2b, while no pores can be observed on the surface as the
172 increase in the laser power up to 200W.

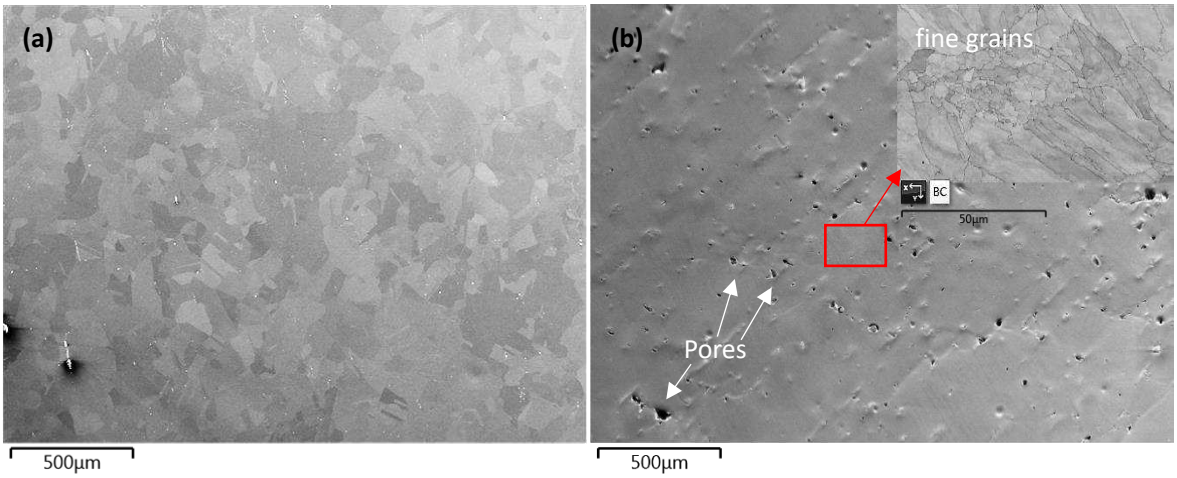

173

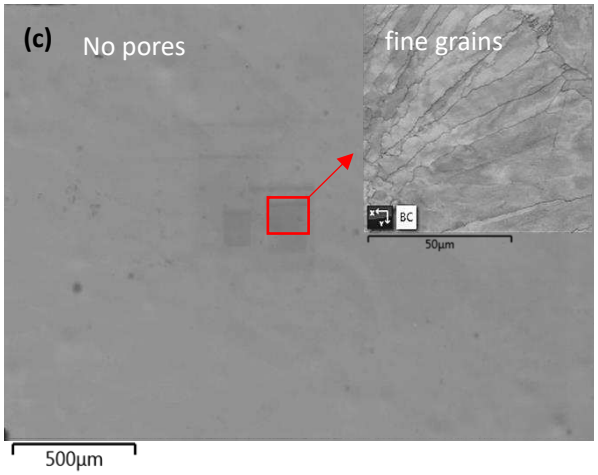

Figure 2. Macrostructure of wrought, DMLS 80W and 200W 316L SS.

In-situ OCP and pH measurements at various immersion times were recorded (Figure 3). For wrought and DMLS 80 W 316L SS, it can be seen that the presence of H_2O_2 causes the fluctuation of OCP in the early stage, follows by a decline and then OCP is maintained stable at -0.16V after the first 5 days of exposure. The stabilised OCP of DMLS 200 W 316L SS after 5 days of exposure was recorded at -0.12 V vs. Ag/AgCl and approx. 50 mV higher than that of wrought and DMLS 80W 316L SS in Stage 1.

The acidifying inflammatory condition in Stage 2 sharply rises the OCP by 200 mV compared to Stage 1, and DMLS 200W 316L SS shows a nobler potential than that of wrought 316L and DMLS 80W 316L SS. The increase in OCP for all types of 316L SS is attributed to the acceleration of the effect of hydrogen ions on the cathodic reaction as follow:

$$H_2O_2 + 2H^+ + 2e^- \rightarrow 2H_2O \qquad (1)$$

The acidification during inflammation provides acidity and promotes reaction (1), further increasing corrosion potential to a higher level.

In Stage 3, the recorded OCP for all types of 316L SS is declined sharply after the removal of

H_2O_2 and the increase of solution pH. It is noted that OCP shifts to relatively negative values compared to that of suffering inflammation, suggesting that the degradation of passive film on 316L SS occurs through the inflammation period in Stage 2.

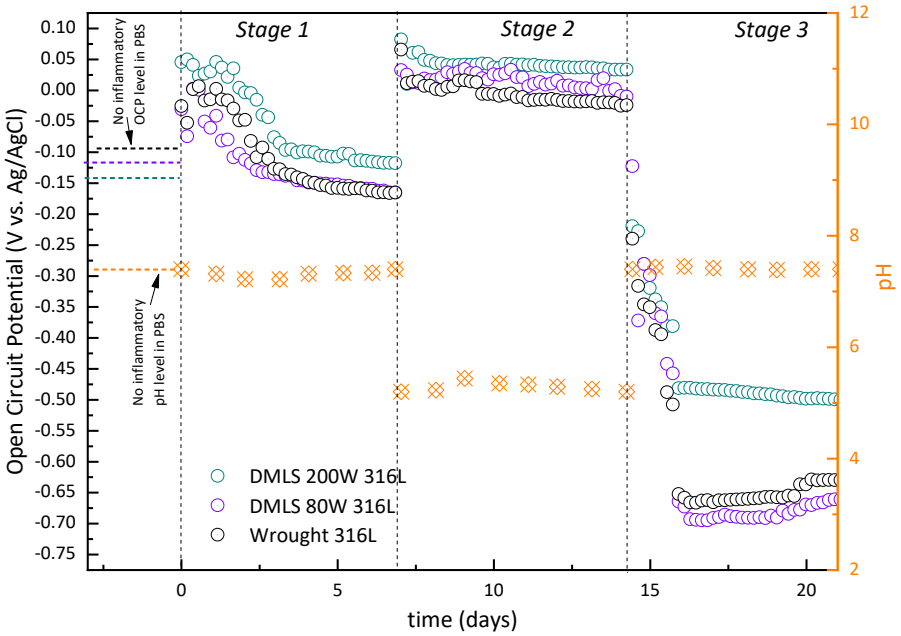

Figure 3. The fluctuation of corrosion potential for wrought, DMLS 80W, and DMLS 200W 316L SS in different stages of simulated inflammation environments.

3.2 Corrosion properties of wrought 316L SS and 3D printed 316L SS exposed to the simulated inflammation environments.

Figure 4 illustrates the passivation behaviour of wrought, DMLS 80W 316L SS and DMLS 200W 316L SS in different simulated body environments. For all three stages, DMLS 200W 316L SS exhibits the most stable passivation behaviour compared to wrought and DMLS 80W 316L SS. It is found that the presence of H_2O_2 at pH 5.2 (Stage 2) increases the current densities for all types of 316L SS, especially for wrought 316L SS. The gradual increase in the current densities suggests that the dissolution rate of the passive film accelerates and beyond its growth rate, leading to the dissolution of the passive film.

The results in Figure 4d indicate that the breakdown potentials considerably reduce for each material after the presence of H_2O_2 at pH 5.2. The breakdown potential for DMLS 200W 316L SS is above 800 mV vs. Ag/AgCl compared to 400 mV vs. Ag/AgCl for wrought 316L in an acidified inflammatory environment. The breakdown potentials of DMLS 80W and 200W 316L SS increase to 1000 mV vs. Ag/AgCl in Stage 3. The elevated breakdown potentials for DMLS 316L SS at high laser power indicate the improved response of the passive film resistance in the simulated inflammation solutions.

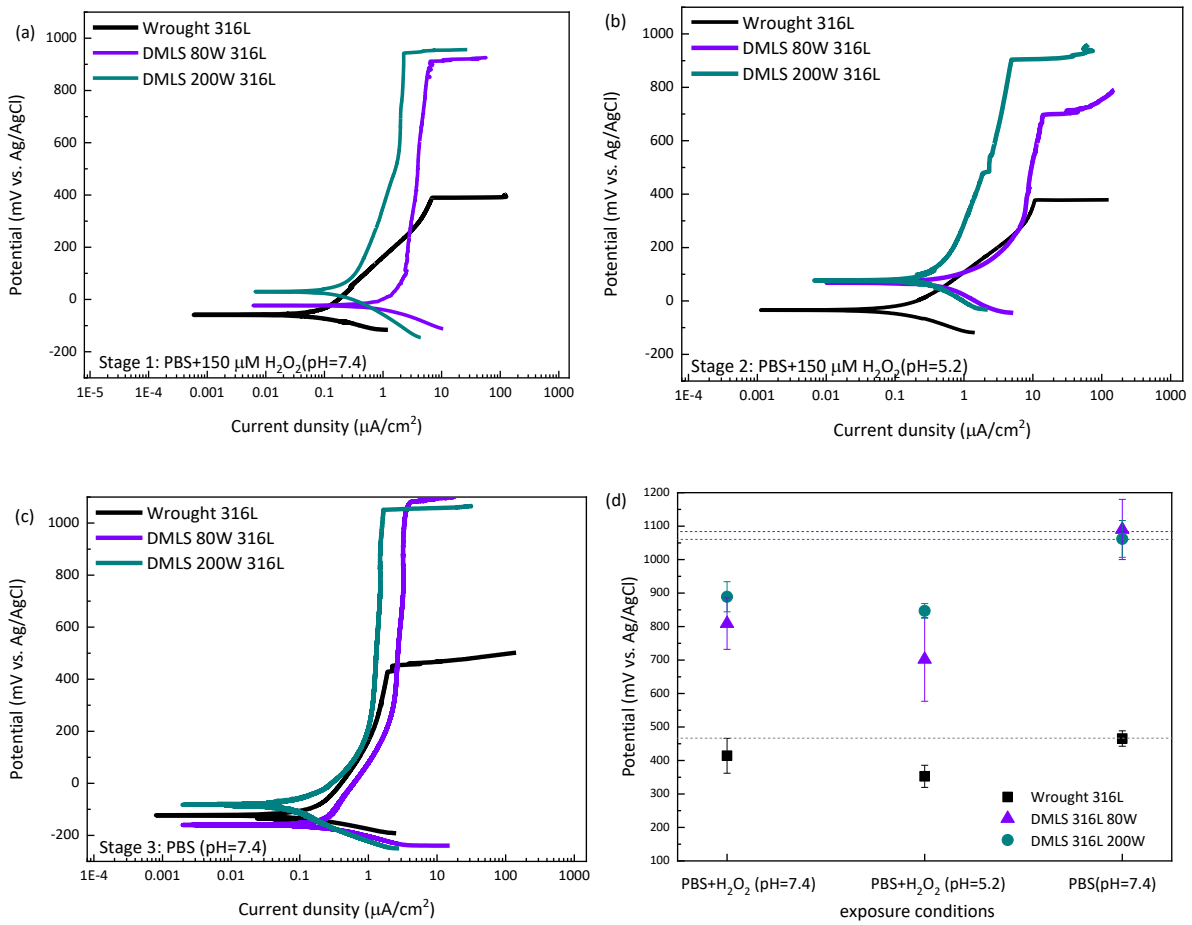

Figure 4. Plots of potential dynamic curves for wrought and DMLS 316L SS in (a) PBS with H_2O_2 at pH 7.4, (b) PBS with H_2O_2 at pH 5.2, (c) PBS without H_2O_2 at pH 7.4 [36]**, and (d) the comparison of pitting potentials for three types of 316L SS in three typical conditions.**

The corrosion behaviour of wrought and DMLS 316L SS at all three stages was continuously measured via EIS as shown in Figure 5 and Figure S1. For Stage 1, the results in Figures 5a-b

show that the semi-circles for wrought and DMLS 316L SS become smaller in the presence of H_2O_2, which indicates that the corrosion resistance gradually decreases with exposure times. DMLS 200W 316L SS shows the largest semi-circle after 7 days of exposure, suggesting the slow dissolution process with fewer released toxic ions.

After a pH drop in Stage 2 as shown in Figure 5c-d, It is interesting to note that the impedance for all types of 316L SS increase after 3 days of exposure to inflammation condition and remain stable thereafter (Table S2). However, the corrosion resistance of DMLS 200W 316 L SS is larger than that of wrought and DMLS 80W 316L SS (Figure S1 b). The large semi-circles for DMLS 200W 316L SS suggest an improved corrosion resistance compared with 316L SS manufactured by wrought process.

Stage 3 illustrates the condition after the removal of H_2O_2 and with the solution pH of 7.4. A linear tail gradually appears in the low-frequency region of Nyquist plots, which suggests that the dissolution of metal ions is controlled by diffusion. The linear tail is due to the evolution of the passive film towards a protective layer with low porosity in nature which acts as a diffusion barrier to inhibit the transportation of the corrosive species to the metal surface with the large charge transfer resistance [42]. The absence of aggressive substances depresses both the cathodic and anodic reactions as shown in Figure 4, leading to the decrease in the dissolution rate of the passive film and a low corrosion current density. During this stage, DMLS 200W 316L represents the highest repassivation ability and the largest impedance compared with that of wrought 316L and DMLS 80W 316L, showing that DMLS 200W 316L SS has the improved corrosion resistance under the test conditions here.

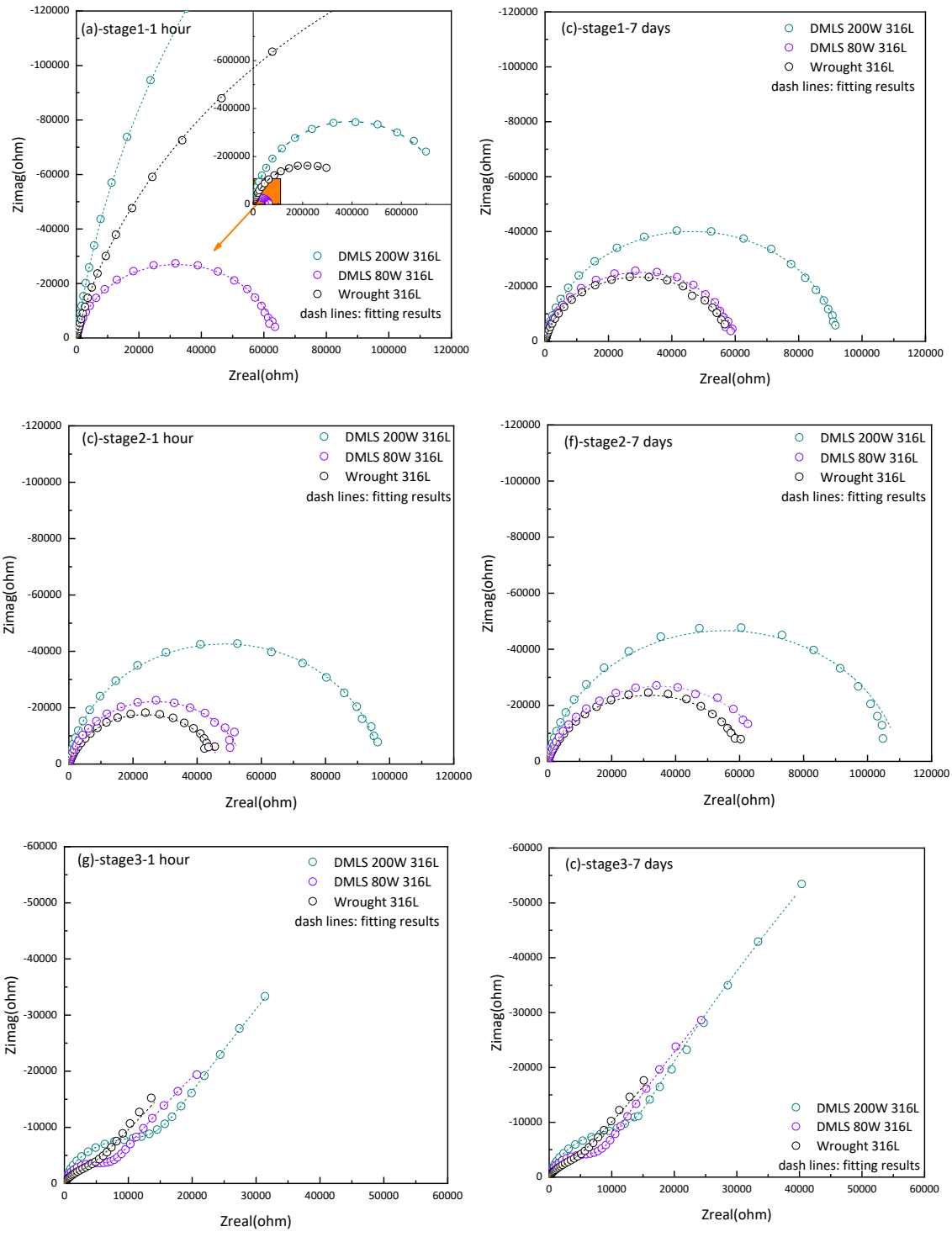

Figure 5. Nyquist plots for wrought 316L SS, DMLS 80W 316L SS, and DMLS 200W 316L SS in simulated inflammation Stage 1 for (a)1 hour and (b) 168 hours, Stage 2 for (c) 1 hours and (d) 168 hours, Stage 3 for (e) 1 hours and (f) 168 hours.

The EIS results were further analysed using the numerical fitting with the equivalent circuit as shown in Figure 6. Two-time constants were applied to characterise the interface for 316L SS,

the semi-conductivity of the passive film with defects (Figure 6a) and a relative dense passive film exhibiting migration phenomena are provided in Figure 6b, where R_s represents the solution resistance, R_{outer} and R_{inner} are the resistance for the outer layer and inner layer of the passive film, and Z_W is the Warburg impedance. CPE1 (Q_{outer}) and CPE2 (Q_{inner}) are used to describe the capacitive behaviours for the outer layer and inner layers. The definition and detailed fitting values are provided in a supplemental document (table S1-S3).

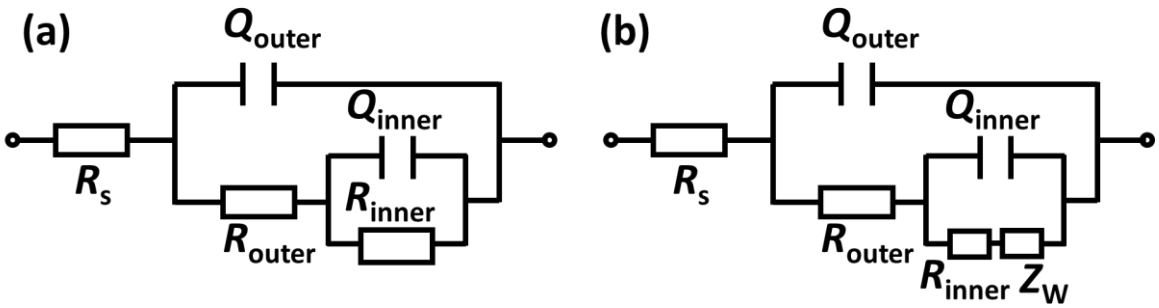

Figure 6. Electrode-equivalent circuits for 316L SS (a) during inflammation period-Stage 1/2 and (b) after inflammation-Stage 3.

The applied electrode-equivalent circuits in Figure 6 suggest the formation of the passive film with defects during the inflammation period, resulting in the penetration of corrosive species through the film to the inner layer. In stages 1 and 2, the resistance of the inner layer mainly corresponds to the charge transfer resistance (R_{ct}), while the growth of the film during Stage 3 is controlled by transport of species (mass transfer, R_{mt}) accompanied by charge transfer through the inner layer. Figure 7a illustrates the resistance against the transport of aggressive ions and toxic metal ions through the inner layer. The square symbols and triangle symbols represent the values of R_{ct} and R_{mt} during inflammation period, respectively. The total resistance for the inner layer was calculated via the following formula and are presented as dash lines in Figure 7a:

$$R_{\mathrm{inner}} = R_{\mathrm{ct}} + R_{\mathrm{mt}} \quad (2)$$

It is noted that the transport of species through the inner layer is promoted after suffering Stage 1 and 2 for both wrought 316L and DMLS 80W 316L SS while the depressing resistance with the removal of inflammation solutions is in Stage 3. Surprisingly, the inner layer resistance of the passive film for DMLS 200W 316L SS reverts to a relatively high level immediately in Stage 3, and gradually raises and approaches the initial level. The enhanced resistance against species transport through the inner layer restricts the release of metal ions from the substrate and suggests the formation of a compact inner layer.

The outer layer of the passive film is regarded as the transformation from the inner layer [42–44]. As shown in Figure 7b, the corrosion resistance of the outer layer (R_{outer}, circle) is relatively insignificant compared with that of the inner layer in stages 1 and 2, whereas showing an exponential increase in Stage 3. The inflammation solution provides an aggressive condition to promote the instability of the inner passive layer, resulting in the accelerating dissolution of the outer layer, indicating as small values of R_{outer}. After the removal of H_2O_2 and the rise of pH in Stage 3, the stability of the passive film is improved with increases in R_{outer}. It is noted that the DMLS 200W 316L SS maintains larger R_{outer} values than wrought 316L SS during the whole period from Stage 1 to Stage 3, which give a passive potential to decrease the dissolution of the passive film and provide a hypo-toxicity.

The total resistance for the passive film was calculated via the following formula and was compared in Figure 7b with the solid line:

$$R_{\mathrm{total}} = R_{\mathrm{inner}} + R_{\mathrm{outer}} \quad (3)$$

The value of R_{total} represents the ability to prevent the toxic metal ions released from the substrate. The passive film formed on DMLS 200W 316L SS exhibits a relatively high resistance during each stage of the inflammation process. DMLS 80W 316L SS represents the improved corrosion resistance compares to wrought 316L SS in all three stages. However, the degradation of the passive film for DMLS 80W 316L in Stage 1 occurs rapidly in the presence of H_2O_2, and this can be ascribed to the pores formed during the manufacturing process which provide the preferred sites for destruction.

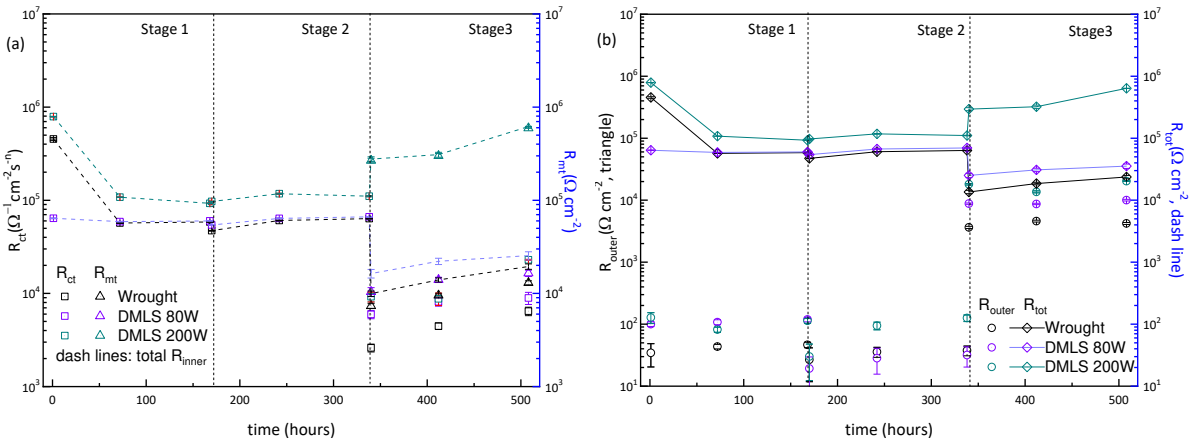

Figure 7. The total resistance for different types of 316L SS through simulated inflammation process

3.2 Post surface characterisation

Characterisation of the passive film

The hypo-toxicity for DMLS 200W 316L SS over the inflammation period reveals the unique passive film as a barrier against metal ions release. Figure 8 shows the different compositions of the passive films formed on wrought, DMLS 80W, and DMLS 200W 316L SS over each stage of inflammation. According to the calculated results of integral areas through XPS peaks, the passive films are mainly constituted by compounds of Fe and Cr with a trace amount of Ni and

Mo compounds.

Figures 8a-c represent the composition of the passive films formed on wrought 316L SS during different stages of inflammation. A high proportion of FeOOH is observed after H_2O_2 infusion, which is believed to converse from Fe_3O_4 and cause the degradation of the passive film [45]. After pH declines in Stage 2, Mo compounds are found in the passive film with the decrease of oxide compounds for Fe, Cr and Ni, which refer to a risk of implants. As the depletion of inflammatory species (Stage 3), Ni stabilises within the passive film and the increased MoO_4^{2-} in Stage 3 are benefited for passivation behaviours through depressing the absorption of Cl^- ions on the sample surface [46].

Figure 8d-f and Figure 8g-I indicate the composition variations of the passive film for DMLS 80W and 200W 316L SS during the inflammation process respectively. The formation of FeOOH is depressed in Stage 1, as well as the reduction in the metallic phase of Fe and Cr for DMLS 316L SS in Stage 2 and Stage 3 compared to wrought 316L SS. The presence of Cr_2O_3 and Ni compounds is responsible to provide high corrosion resistance of the passive film in Stage 3 for DMLS 200W 316L and DMLS 80W 316L, whereas the ratio of the metallic Fe and Cr to Cr_2O_3 and Ni remains high for wrought 316L SS at the end of Stage 3. The presence of Cr_2O_3 and Ni compounds enhances passivation behaviour for DMLS 200W 316L SS, therefore, showing the prominent depression effect on toxic ions release.

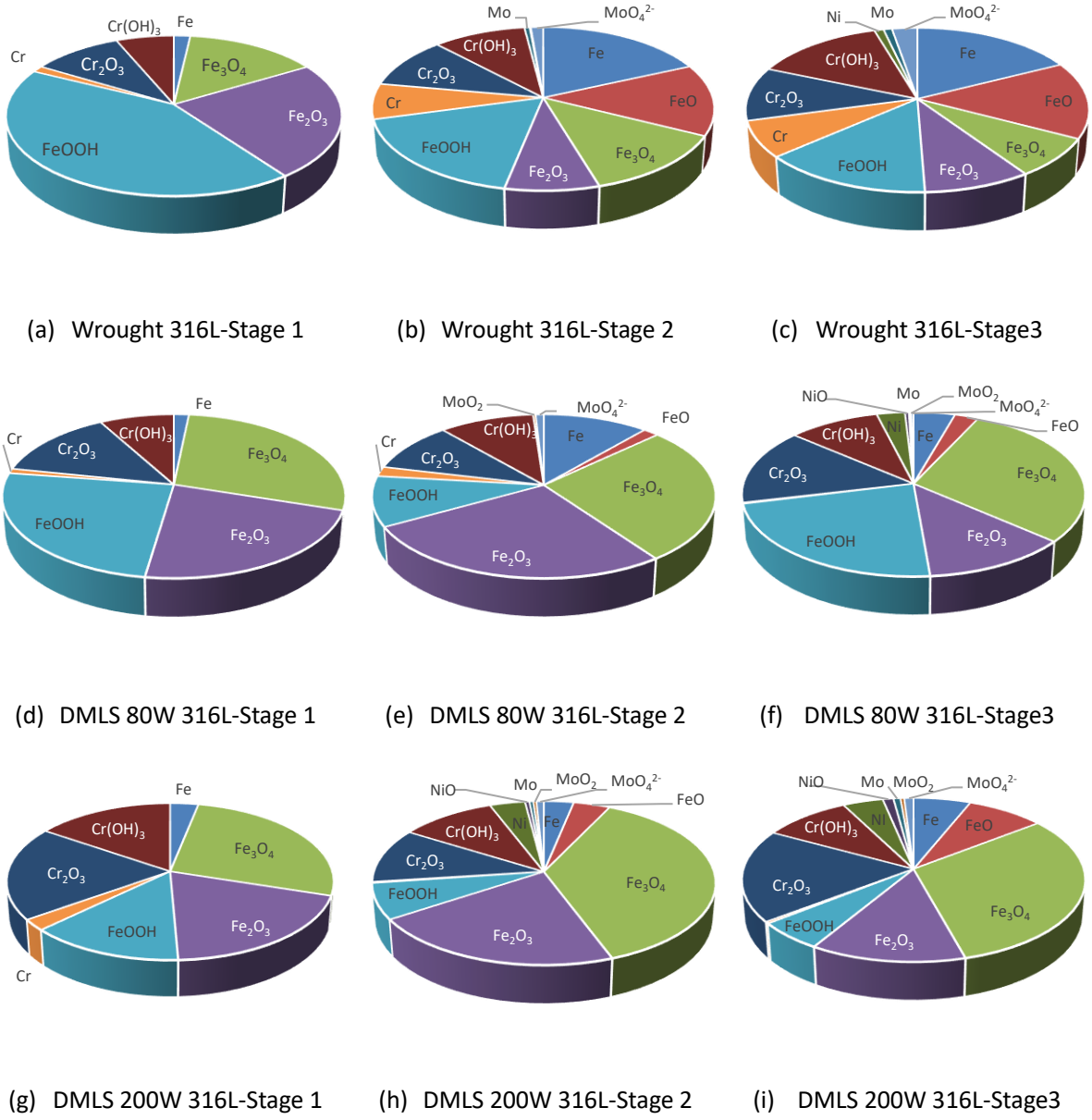

(a) Wrought 316L-Stage 1 (b) Wrought 316L-Stage 2 (c) Wrought 316L-Stage3

(d) DMLS 80W 316L-Stage 1 (e) DMLS 80W 316L-Stage 2 (f) DMLS 80W 316L-Stage3

(g) DMLS 200W 316L-Stage 1 (h) DMLS 200W 316L-Stage 2 (i) DMLS 200W 316L-Stage3

Figure 8. The components of the passive film formed on (a)-(c) wrought 316L, (d)-(f) DMLS 80W 316L, and (g)-(i) DMLS 200W 316L in different stages of simulated inflammation environments.

3.2 Characterisation of the release of metal ions for toxicity from solutions

Characterisation of the passive film reflects the cathodic and anodic reactions affecting by inflammation conditions, and this yields the different migration of the matrix towards the simulated inflammation solutions for wrought and DMLS 316L SS. The dissolution of Fe, Cr, and Ni ions are considered as toxicity in body fluids. Figure 9 illustrates the measured

concentration of Fe, Cr, Ni, and Mo for wrought 316L and DMLS 316L SS from solution at each stage. It is noted that the release of metal ions is relatively high in Stage 2, indicating the accelerated dissolution in the presence of H_2O_2 at low pH. The results are consistent with the obtained polarisation data, where the increase in the current densities was recorded for all three 316L SS samples as shown in Figure 4.

The Ni ions with a high concentration release from wrought 316L SS can be attributed to the absence of solid Ni compounds within the passive film compared with 316L SS manufactured by the DMLS process (Figure 8). Figure 9d provides the total released ions during the whole simulated inflammation period. The DMLS 200W 316L exhibits minimal toxicity during the inflammation process, followed by DMLS 80W 316L. The wrought 316L SS shows the worst behaviours over 21 days immersion test, releasing 0.179 ppm of Ni ions into the simulated inflammation body fluids.

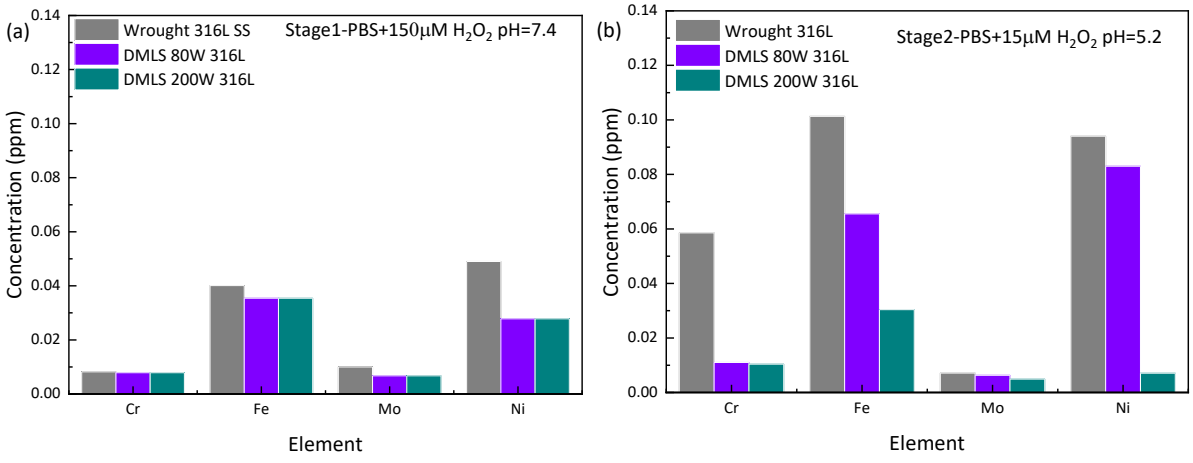

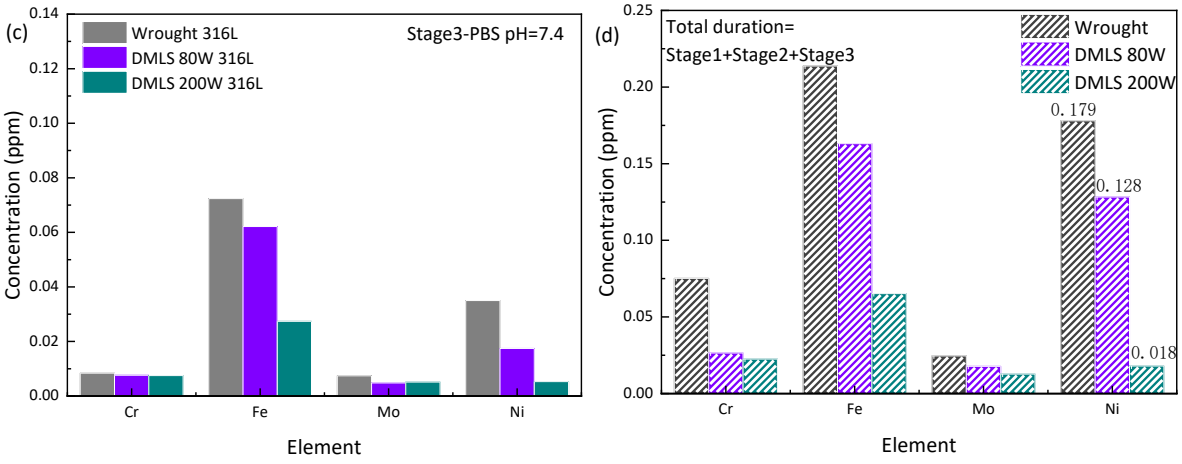

Figure 9. The release of Cr, Fe, Mo, and Ni from wrought and DMLS 80/200W 316L SS in (a) Stage 1, (b) Stage 2, and (c) Stage 3 of inflammation, and (d) the comparison of total ions release between wrought 316L and DMLS 316L.

3.4 The effect of DMLS 316L SS porosity on the development of pit

3.4.1 The effect of pores on the corrosion behaviour

As showed in Figure 2b, many pores were observed on DMLS 80W 316L SS via SEM. To clarify the effect of porosity characteristics of wrought and DMLS 316L SS on the development of local pit, Figure 10 shows that the cyclic polarisation was applied on the different 316L SS samples at the end of both Stage 1 and Stage 2 conditions.

By the end of Stage 1, the passive films formed on wrought 316L and DMLS 80W 316L SS fail to re-passivate, indicating that the reversed anodic curves are intersected to the cathodic curves (Figure 10a) after the passive film breakdown in the presence of H_2O_2. It is interesting to note that the backswept curve for DMLS 200W 316L intersects above corrosion potential, showing that DMLS 200W 316L SS is re-passivated. However, a short potential range between corrosion potential and repassivation potential was observed, corresponding to where restrains the propagation of the existing pits.

For the situation suffering at Stage 2 (Figure 10b), DMLS 80W and 200W 316L SS show

relatively higher breakdown potentials with depressing current density compared to that of wrought 316L SS, especially for 200W. However, the passive films for all types of 316L SS fail to re-passivate after the breakdown, intersecting the curves below OCP to the cathodic curves in the acidified inflammation condition.

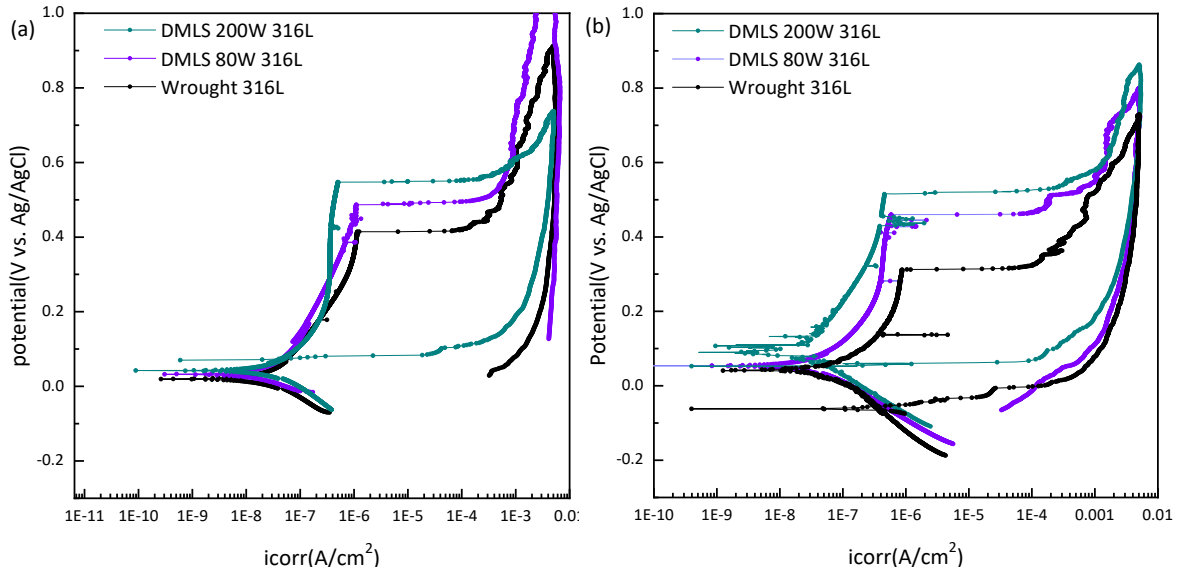

Figure 10. Plots of cyclic polarisation curves for wrought, DMLS 80W, and DMLS 200W 316L SS at the end of Stage 1 (a) and Stage 2 (b).

3.4.2 Surface pit morphology

Figures 11 (a)-(c) and (g)-(i) provide surface morphologies of different types of 316L SS before cyclic polarisation at the end of Stage 1 and Stage 2, respectively. No obvious corrosion product exists, and the polishing marks are visible on the surface. However, some pores can be observed on the surface of DMLS 80W 316L SS.

Figures 11 (d)-(f) and (j)-(l) indicate the surface morphologies of wrought and DMLS 316L SS after the cyclic polarisation measurements, which are the same scanned areas as indicated in Figures 11 (a)-(c) and (g)-(i). The purpose of the tests is to reveal the pores induce the pit growth on the surface in an inflammation condition, especially for DMLS 80W 316L SS. After

the cyclic polarisation at the end of Stage 1, it is interesting to note that some initial pores on the surface of DMLS 80W 316L SS develop into pitting which has been marked as the red square (Figure 11d). For Stage 2, large pits are developed after the cyclic polarisation measurement, and the location is closed to the pores, as showed in Figure 11j. For wrought and DMLS 200W 316L SS, the surfaces are clean, no pores can be found on the surface before the cyclic polarisation. However, pittings are developed randomly on the surface after applying cyclic polarisation.

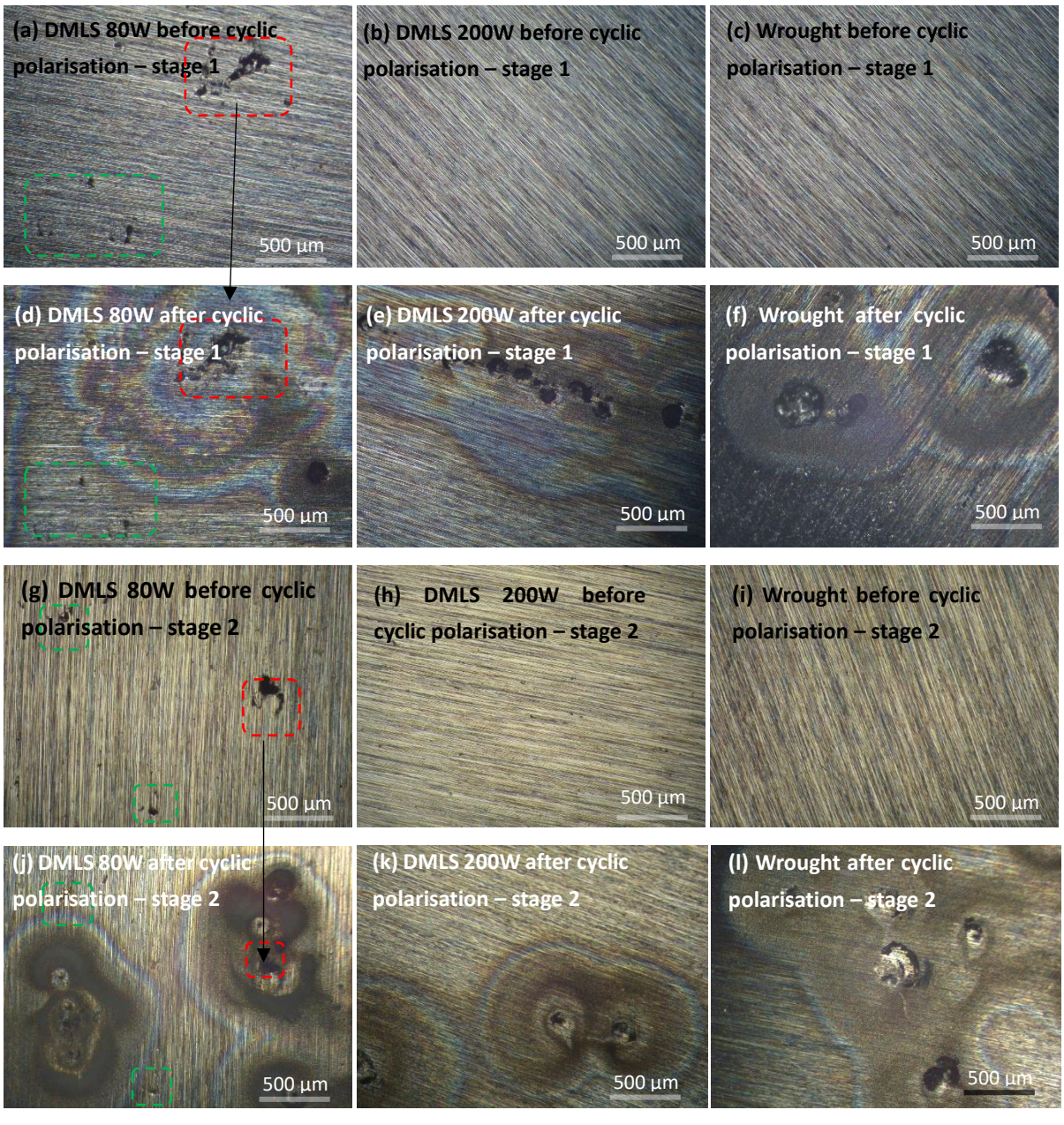

Figure 11. Morphology of the sample surface before and after polarisation.

3.4.3 The effect of pores on the pit propagation

To further investigate the effect of pores on the propagation of pitting corrosion, DMLS 80W 316L SS was selected and the sample was immersed in the solution and applied with a constant potential of 600 mV vs. Ag/AgCl (beyond the breakdown potential for DMLS 80W 316L).

Figure 12 illustrates the surface morphology before and after applying a constant potential of 600 mV vs. Ag/AgCl (current-time curves are shown in Figure S2), and the pit morphology and pit depth were measured via SEM and profilometry measurements. The average pit depths in Figure 12c were calculated by considering the top 10 deepest pits from the sample surface. In the region shown in Figures 12 a and b, pore 1 increases from 24.6 to 42.7 µm between 0 and 4000s, corresponding to the average pit depth of 35.5 µm; this suggests that initial pores have the potential to promote the pit growth on the surface. Interestingly, the pore depths (labeled as number 2 and 3 in Figure 11b) maintain relatively stable before and after the polarisation measurements, the pore depths of 33.8 and 27.2 µm were measured after 4000s at the static polarisation of 600 mV vs. Ag/AgCl.

406

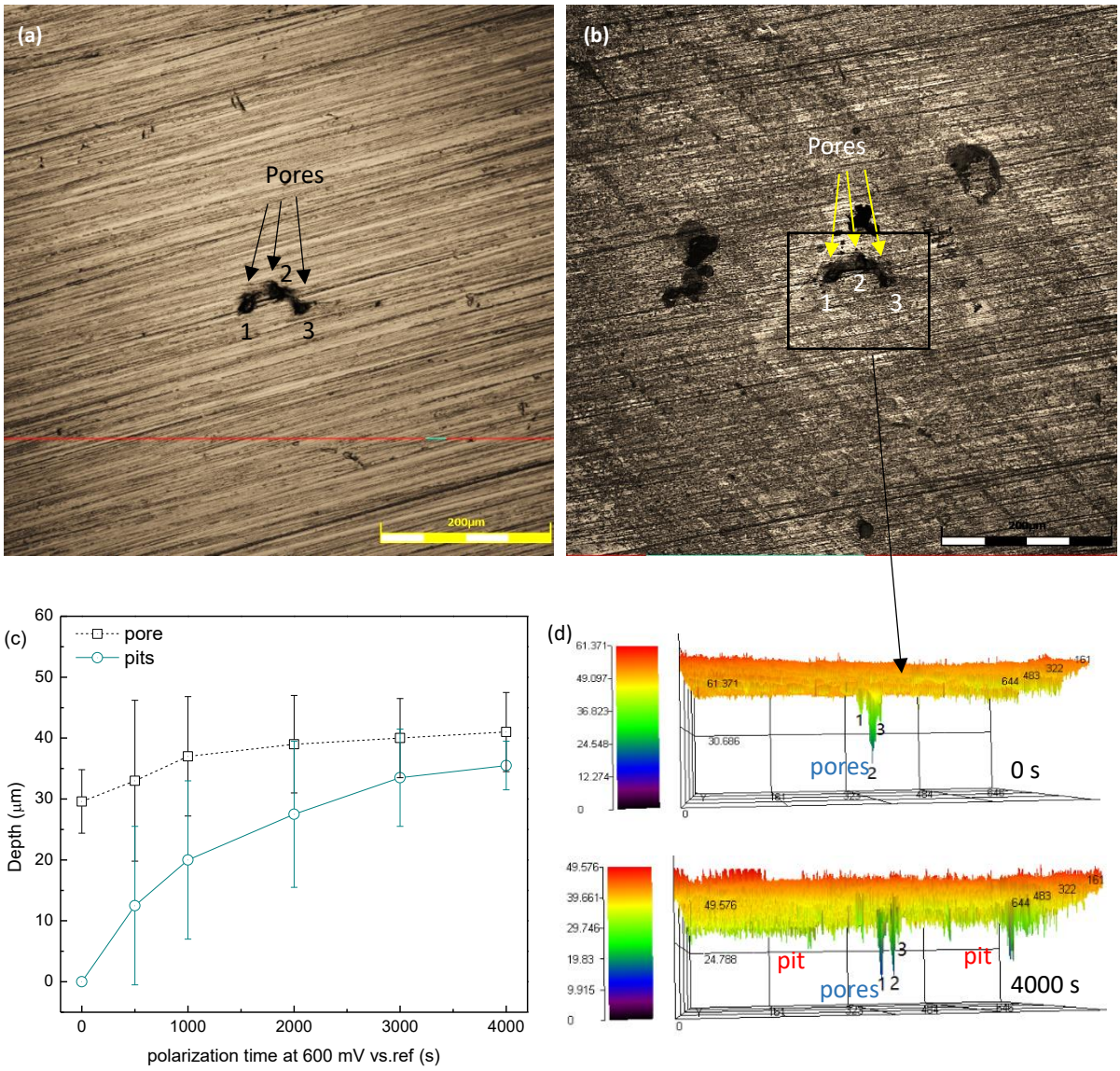

407

408 **Figure 12. Morphology on the surface of DMLS 80W 316L SS at the static polarisation of**
409 **600 mV vs. Ag/AgCl for (a) 0s and (b) 4000s; and the (c) average depth and (d) profilometry**
410 **of the prores and pits in the period of Stage 1.**

411 Figures 13a and 13b illustrate the polarised surface morphology in the acidised inflammation
412 solution (Stage 2) for 0s and after 4000s. It is noted that the morphology of pores shows
413 obvious changes, and the pore sizes increase with the polarised time prolong (blue area). The
414 average pit depth by profilometry measurements is shown in Figure 13c. The large deviation
415 for pit depth is attributed to the uniformed growth for the initial pores. As shown in Figure

13d, pore 1 increases in depth significantly whereas pore 2 shows inactivity during applying the potential, presenting the similar characteristics for DMLS 80W 316L in Stage 1.

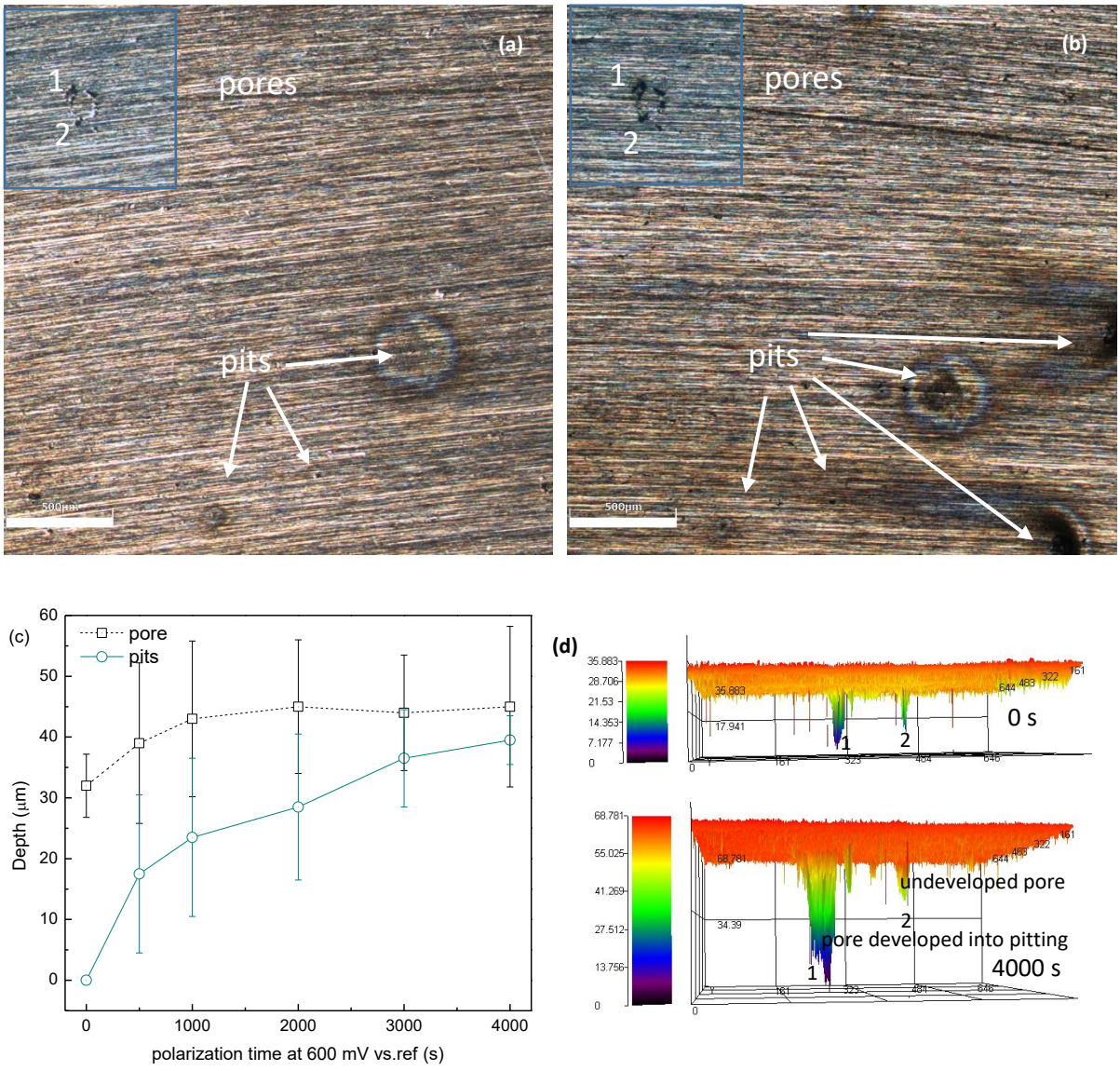

Figure 13. Morphology on the surface of DMLS 80W 316L SS at the static polarisation of 600 mV vs. Ag/AgCl for (a) 0s and (b) 4000s; and the (c) average depth and (d) 3D profilometry of the prores and pits in the period of Stage 2.

4.0 Discussions

Based on the results above, DMLS 200W 316L SS suffers less corrosion attack in a simulated inflammation body environment, followed by DMLS 80W 316L then wrought 316L SS. The

passive film properties are influenced by acidification and the presence H_2O_2 within the PBS solution, especially the latter one. The presence of H_2O_2 plays an important role in the influence of passive film properties and corrosion behaviour for application of DMLS 316L SS as an implant material.

4.1 Passive film properties

Figure 14 summaries the breakdown potentials of the passive film under different stages of simulated inflammation environments. The protective performance of the passive film is remarkable for DMLS 316L SS, and the breakdown potentials are higher than that for wrought, leading to an improved passivation behaviour.

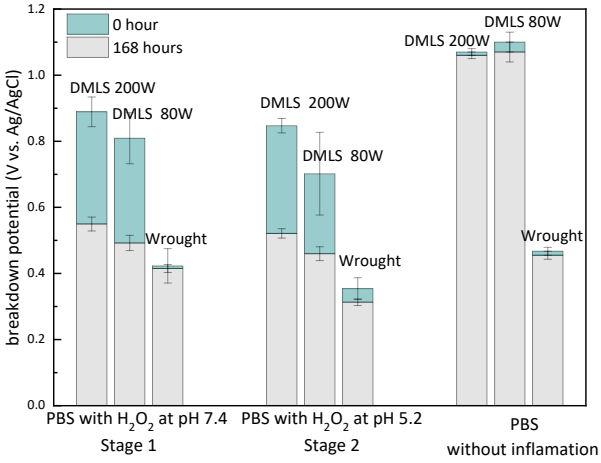

Figure 14. Breakdown potential for wrought, DMLS 80W, and DMLS 200W 316L SS under different stages of simulated inflammation environments.

The composition differences between the passive films formed in the natural body environment and inflammation body environment are mainly attributed to the presence of H_2O_2. In Stage 1, Fe dissolution is faster compared with Cr, and a large amount of Fe^{2+} ions release as shown in Figure 9. The XPS analyses (Figure 8) indicates that the surface film is dominated by the oxidation of Fe and the presence of H_2O_2 contributes to the formation of

the passive film as follows:

$$2Fe^{2+} + H_2O_2 + 2H_2O \leftrightarrow 2FeOOH + 4H^+ \quad (4)$$

$$2Fe^{2+} + H_2O_2 + H_2O \leftrightarrow Fe_2O_3 + 4H^+ \quad (5)$$

$$3Fe^{2+} + H_2O_2 + 2H_2O \leftrightarrow Fe_3O_4 + 6H^+ \quad (6)$$

It is noted that the electron acquisition capability for H_2O_2 promotes the formation of iron oxides with high valence. Among them, the passive film formed on DMLS 316L SS presents low hydrated feature compared with wrought 316L SS with the presence of H_2O_2 in the simulated inflammation environment of Stage 1 and Sage 2, favouring formation of Fe_3O_4 rather than FeOOH. The formation of Fe_3O_4 consumes ferrous ions, indicating a depressed dissolution current density on the surface of DMLS 316L SS by the preference of reaction (6), which in agreement with XPS results shown in Figure 8.

Unlike Fe compounds, the presence of H_2O_2 has less impact on the formation of Cr compounds, considering the stable valence for thermodynamically stable compounds:

$$2Cr^{3+} + 6H_2O \leftrightarrow 2Cr(OH)_3 + 6H^+ \quad (7)$$

$$2Cr^{3+} + 3H_2O \leftrightarrow Cr_2O_3 + 6H^+ \quad (8)$$

Cr_2O_3 regarded as the effective compounds for passivation [47] and shared a similar structure with Fe_3O_4 [48]; however, their proportion decreases in the passive film in the simulated inflammation environment of Stage 2 due to the acidification of the solution. The detection of metallic phase as shown in Figures 8b and 8e suggest that the development of the passive film on the surface is suppressed and accompanied by an accelerated dissolution rate in an

463 acidised inflammation environment (Figure 9b), especially for wrought 316L SS.

464 Considering the high proportion of FeOOH for Stage 1, the corrosion reaction of the passive
465 film is mainly attributed to the following reaction

$$(2x + y)FeOOH + 3yH^{+} \leftrightarrow xFe_2O_3 + (x + 2y)H_2O + yFe^{3+} \quad (9)$$

466 For wrought 316L SS, unstable FeOOH prefers to dissolve to soluble ions than forming solid
467 iron oxide, showing as a low amount of Fe_2O_3 within the passive film and a high level of Fe
468 ions release. However, the passive film of DMLS 316L SS contains more iron oxide in acidifying
469 inflammation conditions consequently releases fewer Fe ions and showed hypo-toxicity and
470 prominent passivation characteristics, especially for the samples manufactured at 200W.

471 ***4.2 Toxicity analysis of the solution at each stage***

472 Steinemann [49] proposed that the toxicity of the implant materials is associated with metal
473 ion dissolution and its subsequent reaction products, such as high solubility hydroxides and
474 hydrous oxides. According to the results obtained by Yamamoto et al., [50] Fe and Cr salts,
475 which are metallic hard acids, have relatively low cytotoxicity, whereas the released Ni cations
476 are corresponding to middle cytotoxicity.

477 As shown in Figures 15a and b, the oxides of Cr and Fe remain thermodynamically stable at a
478 neutral pH condition, presenting as Cr_2O_3 and Fe_2O_3/Fe_3O_4, consistent with the results
479 obtained by Man et al. [38,51]. The presence of Cr_2O_3 coexists with $Cr(OH)_3$ which has low
480 solubility in the aqueous phase, suggesting the depressed dissolution of Cr compounds and
481 low cytotoxicity inducing by Cr ions release.

$$Cr_2O_3 + 3H_2O \leftrightarrow 2Cr(OH)_3 \quad (10)$$

For Fe^{2+} ions, the precipitation of FeOOH can reduce the dissociation of Fe_2O_3 at an elevated potential. Fe_3O_4 and Fe_2O_3 coexist with soluble ions in a wide potential range as reactions (11) and (12), which results in the relatively high release of Fe^{2+} species but not dominate the toxicity due to the low cytotoxicity of iron ions.

$$Fe_2O_3 + 6H^+ \leftrightarrow 2Fe^{3+} + 3H_2O \quad (11)$$

$$Fe_3O_4 + 8H^+ \leftrightarrow Fe^{2+} + 2Fe^{3+} + 4H_2O \quad (12)$$

Figure 15c represents the Pourbiax diagram for Ni in 316L SS which is regarded as toxicity for implants [30,31]. NiO directly dissolves as soluble Ni^{2+} ions in the equilibrium reaction (13) in the aqueous phase, resulting in the high release of Ni^{2+}.

$$NiO + 2H^+ \leftrightarrow Ni^{2+} + 2H_2O \quad (13)$$

Besides, the formation of oxides and hydroxides (reaction (4)-(8)) consumes alkalinity and results in the decrease in pH on the surface, promoting the release of Ni ions where localised acidification occurs.

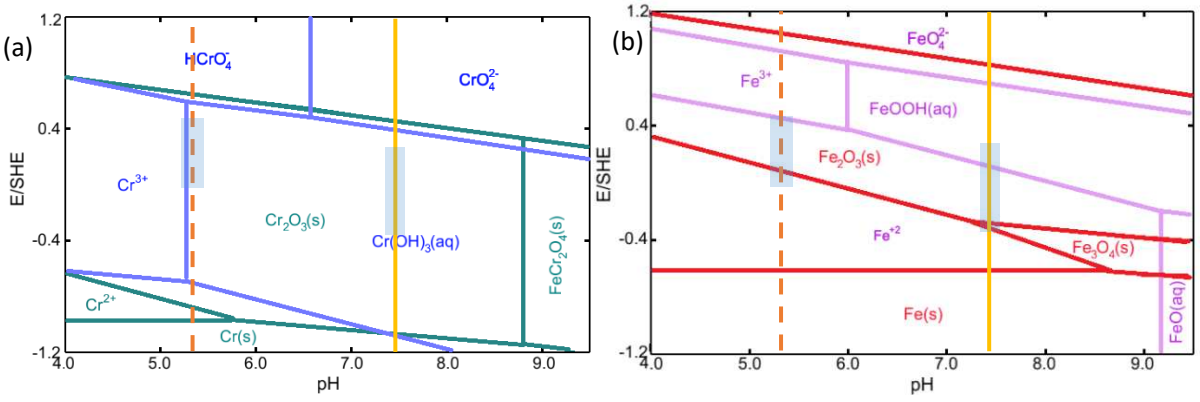

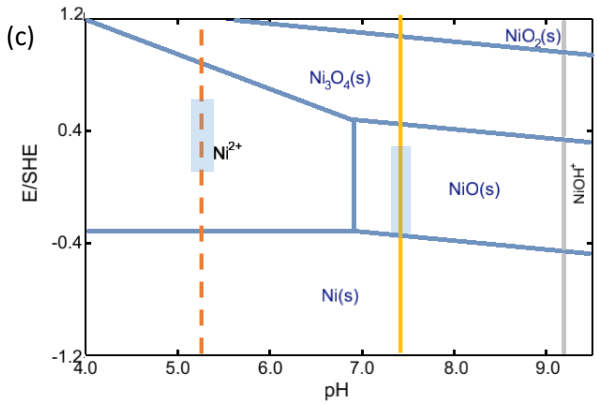

Figure 15. Pourbiax diagram of (a) Cr, (b) Fe, and (c) Ni in 316L SS in Stage 2.

During the whole inflammation process, Stage 2 is noted as the most severe condition for implant material due to the acidification condition, which is also reflected by Pourbiax diagram showing as dash lines in Figure 15. The oxide of Cr coexists with its hydroxide at the pH of 5.2, whereas tends to dissolve into ions when the localised pH decreases below 5.15. Fe_2O_3 coexists with Fe ions, however, it cannot maintain thermodynamically stability in local areas at low corrosion potential, corresponding to the increase in ion release in this period.

As for Ni, no solid compound is thermodynamically stable at pH 5.2. The Ni compounds dissolve soluble ions when immersed in the acidised solution in Stage 2. The ICP results shown in Figure 9b indicate the thermodynamically stability of Ni^{2+} ions and the higher dissolution occurring on the surface of wrought 316L SS. DMLS 316L SS suppressed toxicity release in Stage 2, especially for 200W samples, suggesting the barrier effect of the passive film against the penetration of corrosive ions, and the results are consistent with the passivation characteristics above.

Refer to the analyses for the composition of the passive film formed on DMLS 200W 316L SS in the simulated inflammation solution (Figure 8g and h), the large amount of sub-grain

boundaries (high-density dislocation and Cr/Mo segregation) provides the pathway and recovers the passive film on the surface of DMLS 200W SS [38,52,53]. The growth of Cr_2O_3 protects the surface of DMLS 200W 316L and results in the Fe and Ni compounds maintaining stationary components after 168 hours of immersion in Stage 2. The Ni compounds involved in the passive film further depress the metal ion release and reduce the toxicity during implantation compared with wrought 316L SS.

4.3 Effect of porosity on the pit properties

The DMLS process provides the potential of implants to have hypo-toxicity behaviour, especially after clarifying the corrosion issues that may restrict application. It has been well known that the development of pitting corrosion due to the local acidified at the material interface greatly increased the ion release [4,5], as well as concentrated the stress and led to implant failure [54]. Frankel et al. [55] proposed that pitting corrosion would occur if the dissolution rate (R_{dis}) within the pits/pores kept beyond cations diffusion rate (R_{diff}), and this suggests a critical cation concentration (C_{crit}) for pit propagation. DMLS 316L SS shows better passivation behaviours than wrought 316L. The ICP results as shown in Figure 9 reveal the low R_{dis} for DMLS 316L SS at both laser powers. The active dissolution current (i_{dis}), which neglects the total ohmic potential drop between substrate and solution, and is written as follow to reflect the R_{dis} [56]:

$$i_{dis} = i_{corr} \cdot \exp\left(\frac{E_{app} - E_{corr}}{\beta_a}\right) \quad (14)$$

where E_{app} represents the applied potential for the active dissolution, and i_{corr}, E_{corr}, and β_a are the potential, corrosion current, and anode Tafel slope for the substrate, respectively.

Therefore, the value of i_{dis} at 600 mV vs. Ag/AgCl is large and results in the stable pit growth. It has been noted that the E_{corr} for DMLS 316L SS is significant nobler than that for wrought 316L SS immersed in the simulated inflammation environment (Figure 3 and 9), leading to a relatively low dissolution rate at the same E_{app}. Kong et al. [51] tested the volta potential map on the surface of 316L SS via scanning Kelvin probe force microscopy and found the enrichment of Cr and Mo at the sub-grain boundaries raised the potential of 5 mV and promoted the oxidisation of passive film which further elevated the corrosion potentials. The elevated corrosion potentials for DMLS 316L SS suppress the active dissolution rate and result in the reduction of ions release with toxicity, especially for the sample manufactured at 200W. However, it also is noted that the initial pores on the surface of DMLS 80W 316L SS create difficulty for cation diffusion, corresponding to a relatively low R_{diff} due to the complicated pore shape, indicating a low level of C_{crit} within pores which provides the potential to cause pitting corrosion in the simulated inflammation body fluids. Man et al. [57] proposed that the possibility of the pores induced pit growth for DMLS 316L SS in aggressive conditions, consistent with our results as shown in Figure 12 and Figure 13. The acidity release with the active dissolution was believed to attribute to the Cl^- migrates into the pit in order to balance the charge and maintain electroneutrality [56], and the initial pores on the DMLS 316L SS surface provide the advantage of forming an occluded corrosion cell based on the geometric characteristics. The results suggest the growth feature for multiple pores, that are, the pore with the lowest potential continuously dissolves as an anode, while other pores with nobler potentials as cathodes, inhibiting to develop into pitting corrosion. Finally, the formation of the corrosion products can restrict the corrosive species and affect the localised potentials on

555 the surface, the uncovered pore can be considered as an anode site with the lower potentials
556 to develop into pitting corrosion.

557 For the body fluid condition, the low concentration of Cl^- and a certain pH buffer capacity
558 reduce the risk of environmental degradation to the pores; this indicates the prospect for the
559 application of 3D-printed 316L SS as implants under the premise of controlling the quantity
560 and size of pores during the manufacture. However, further work needs to address the
561 mechanical properties and the acceptable pore sizes that can be safely applied to the human
562 environment as implants as well as the improved methods such as suitable laser power that
563 would improve the corrosion behaviour and mechanical properties of DMLS 316L SS for
564 biological applications.

565 ## *5.0 Conclusion*

566 In summary, this study has systematically compared the passivation behaviours and toxicity
567 for wrought 316L and DMLS 316L SS as implants in the early period with inflammation. The
568 evolution and characterisation of the passive film and the pitting initiated by the intrinsic
569 printing-induced pores during the inflammation process was evaluated and the main
570 conclusions can be drawn as follows:

571 1. All types of 316L SS showed the degradation behaviour with the presence of H_2O_2 in an
572 acidic environment. The 316L SS produced by DMLS revealed the improved breakdown
573 potential compared to wrought 316L SS, especially fabricated under high laser power
574 (200W) with high density.

575 2. The passive film formed on DMLS 200W 316L SS acted as a better barrier against the

corrosive species and suppressed metal ion release. The dissolved concentrations of Fe, Cr, Mo, and Ni were at a lower level compared to wrought 316L SS during the whole simulated inflammation period.

3. The favourable of forming Cr_2O_3, Fe_3O_4, and Ni compounds within the passive film on the surface of DMLS 200W 316L are compacted and results in the hypo-toxicity in the simulated inflammation solution.

4. The pores on the surface of DMLS 80W 316L SS promotes the development of pit, inducing serve pitting corrosion and increasing the levels of toxic metal ions in the solution.

Reference

[1] X. Wang, S. Xu, S. Zhou, W. Xu, M. Leary, P. Choong, M. Qian, M. Brandt, Y.M. Xie, Biomaterials 83 (2016) 127–141.

[2] D. Kong, C. Dong, X. Ni, X. Li, Npj Mater. Degrad. 3 (2019) 24.

[3] G. Sander, J. Tan, P. Balan, O. Gharbi, D. Feenstra, L. Singer, S. Thomas, R. Kelly, J. Scully, N. Birbilis, Corrosion 74 (2018) 1318–1350.

[4] T. Hoar, Corros. Sci. 7 (1967) 341–355.

[5] N. Sato, Electrochimica Acta 16 (1971) 1683–1692.

[6] E. Sikora, D.D. Macdonald, Solid State Ion. 94 (1997) 141–150.

[7] H. Luo, C. Dong, K. Xiao, X. Li, RSC Adv. 6 (2016) 9940–9949.

[8] C. Fonseca, M. Barbosa, Corros. Sci. 43 (2001) 547–559.

[9] E.K. Brooks, R.P. Brooks, M.T. Ehrensberger, Mater. Sci. Eng. C 71 (2017) 200–205.

[10] W. Xu, F. Yu, L. Yang, B. Zhang, B. Hou, Y. Li, Mater. Sci. Eng. C 92 (2018) 11–19.

[11] S.T. Test, S. Weiss, J. Biol. Chem. 259 (1984) 399–405.

[12] M. Atapour, X. Wang, K. Färnlund, I. Odnevall Wallinder, Y. Hedberg, Electrochimica Acta 354 (2020) 136748.

[13] M. Cieślik, W. Reczyński, A.M. Janus, K. Engvall, R.P. Socha, A. Kotarba, Corros. Sci. 51 (2009) 1157–1162.

[14] R. Köster, D. Vieluf, M. Kiehn, M. Sommerauer, J. Kähler, S. Baldus, T. Meinertz, C.W. Hamm, The Lancet 356 (2000) 1895–1897.

[15] Z.-H. Zhao, Y. Sakagami, T. Osaka, Can. J. Microbiol. 44 (1998) 441–447.

[16] X. Zhang, W. Xu, D. Shoesmith, J. Wren, Corros. Sci. 49 (2007) 4553–4567.

[17] W. Xu, F. Yu, L. Yang, B. Zhang, B. Hou, Y. Li, Mater. Sci. Eng. C 92 (2018) 11–19.

[18] C. Fonseca, M. Barbosa, Corros. Sci. 43 (2001) 547–559.

[19] C.N. Kraft, B. Burian, L. Perlick, M.A. Wimmer, T. Wallny, O. Schmitt, O. Diedrich, J. Biomed. Mater. Res.

Off. J. Soc. Biomater. Jpn. Soc. Biomater. Aust. Soc. Biomater. Korean Soc. Biomater. 57 (2001) 404–412.
[20] C.-C. Shih, C.-M. Shih, Y.-Y. Su, L.H.J. Su, M.-S. Chang, S.-J. Lin, Corros. Sci. 46 (2004) 427–441.
[21] M. Metikoš-Huković, Z. Pilić, R. Babić, D. Omanović, Acta Biomater. 2 (2006) 693–700.
[22] K. Asami, K. Hashimoto, S. Shimodaira, Corros. Sci. 18 (1978) 151–160.
[23] T. Zhang, X. Jiang, X. Lu, S. Li, C. Shi, Corrosion 50 (1994) 339–344.
[24] R. Moreira, C. Franco, C. Joia, S. Giordana, O. Mattos, Corros. Sci. 46 (2004) 2987–3003.
[25] J.-B. Lee, S.-W. Kim, Mater. Chem. Phys. 104 (2007) 98–104.
[26] H. Li, C. Yang, E. Zhou, C. Yang, H. Feng, Z. Jiang, D. Xu, T. Gu, K. Yang, J. Mater. Sci. Technol. 33 (2017) 1596–1603.
[27] Y. Hua, S. Mohammed, R. Barker, A. Neville, J. Mater. Sci. Technol. 41 (2020) 21–32.
[28] E.J. Martin, R. Pourzal, M.T. Mathew, K.R. Shull, Langmuir 29 (2013) 4813–4822.
[29] X. Li, Y. Zhao, W. Qi, J. Xie, J. Wang, B. Liu, G. Zeng, T. Zhang, F. Wang, Appl. Surf. Sci. 469 (2019) 146–161.
[30] W.M. Elshahawy, I. Watanabe, P. Kramer, Dent. Mater. 25 (2009) 1551–1555.
[31] R. LAPPALAINEN, A. YLI-URPO, Eur. J. Oral Sci. 95 (1987) 364–368.
[32] L. Navarro, J. Luna, I. Rintoul, Surf. Rev. Lett. 24 (2017) 1730002.
[33] F. Bartolomeu, M. Buciumeanu, E. Pinto, N. Alves, O. Carvalho, F. Silva, G. Miranda, Addit. Manuf. 16 (2017) 81–89.
[34] C. Man, C. Dong, T. Liu, D. Kong, D. Wang, X. Li, Appl. Surf. Sci. 467 (2019) 193–205.
[35] D. Kong, X. Ni, C. Dong, X. Lei, L. Zhang, C. Man, J. Yao, X. Cheng, X. Li, Mater. Des. 152 (2018) 88–101.
[36] X. Yue, L. Zhang, Y. Hua, J. Wang, N. Dong, X. Li, S. Xu, A. Neville, Appl. Surf. Sci. 529 (2020) 147170.
[37] N.S. Al-Mamun, K. Mairaj Deen, W. Haider, E. Asselin, I. Shabib, Addit. Manuf. 34 (2020) 101237.
[38] C. Man, C. Dong, T. Liu, D. Kong, D. Wang, X. Li, Appl. Surf. Sci. 467 (2019) 193–205.
[39] E.K. Brooks, R.P. Brooks, M.T. Ehrensberger, Mater. Sci. Eng. C 71 (2017) 200–205.
[40] S.T. Test, S. Weiss, J. Biol. Chem. 259 (1984) 399–405.
[41] ASTM G61, Cyclic Potentiodynamic Polarization Testing, ASTM international, 1999.
[42] C. Boissy, C. Alemany-Dumont, B. Normand, Electrochem. Commun. 26 (2013) 10–12.
[43] J.O. Bockris, D. Drazic, Electrochimica Acta 7 (1962) 293–313.
[44] C.-O. Olsson, D. Landolt, Electrochimica Acta 48 (2003) 1093–1104.
[45] X. Zhang, W. Xu, D. Shoesmith, J. Wren, Corros. Sci. 49 (2007) 4553–4567.
[46] Y. Wang, X. Cheng, X. Li, Electrochem. Commun. 57 (2015) 56–60.
[47] V. Maurice, W. Yang, P. Marcus, J. Electrochem. Soc. 145 (1998) 909–920.
[48] B. Zhang, J. Wang, B. Wu, X. Guo, Y. Wang, D. Chen, Y. Zhang, K. Du, E. Oguzie, X. Ma, Nat. Commun. 9 (2018) 2559.
[49] S.G. Steinemann, Implants Infect. Fract. Fixat. 27 (1996) S/C16-S/C22.
[50] A. Yamamoto, R. Honma, M. Sumita, J. Biomed. Mater. Res. 39 (1998) 331–340.
[51] D. Kong, C. Dong, X. Ni, L. Zhang, H. Luo, R. Li, L. Wang, C. Man, X. Li, Appl. Surf. Sci. 504 (2020) 144495.
[52] C. Man, Z. Duan, Z. Cui, C. Dong, D. Kong, T. Liu, S. Chen, X. Wang, Mater. Lett. 243 (2019) 157–160.
[53] D. Kong, C. Dong, S. Wei, X. Ni, L. Zhang, R. Li, L. Wang, C. Man, X. Li, Addit. Manuf. 38 (2021) 101804.
[54] X. Yue, M. Zhao, L. Zhang, H. Zhang, D. Li, M. Lu, RSC Adv. 8 (2018) 24679–24689.
[55] G.S. Frankel, T. Li, J.R. Scully, J. Electrochem. Soc. 164 (2017) C180–C181.
[56] T. Li, J.R. Scully, G.S. Frankel, J. Electrochem. Soc. 165 (2018) C762–C770.
[57] Z. Duan, C. Man, C. Dong, Z. Cui, D. Kong, L. wang, X. Wang, Corros. Sci. 167 (2020) 108520.

653